

Higher-than-predicted saltation threshold wind speeds on Titan

Devon M. Burr¹, Nathan T. Bridges², John R. Marshall³, James K. Smith⁴, Bruce R. White⁵ & Joshua P. Emery¹

Titan, the largest satellite of Saturn, exhibits extensive aeolian, that is, wind-formed, dunes^{1,2}, features previously identified exclusively on Earth, Mars and Venus. Wind tunnel data collected under ambient and planetary-analogue conditions inform our models of aeolian processes on the terrestrial planets^{3,4}. However, the accuracy of these widely used formulations in predicting the threshold wind speeds required to move sand by saltation, or by short bounces, has not been tested under conditions relevant for non-terrestrial planets. Here we derive saltation threshold wind speeds under the thick-atmosphere, low-gravity and low-sediment-density conditions on Titan, using a high-pressure wind tunnel⁵ refurbished to simulate the appropriate kinematic viscosity for the near-surface atmosphere of Titan. The experimentally derived saltation threshold wind speeds are higher than those predicted by models based on terrestrial-analogue experiments^{6,7}, indicating the limitations of these models for such extreme conditions. The models can be reconciled with the experimental results by inclusion of the extremely low ratio of particle density to fluid density⁸ on Titan. Whereas the density ratio term enables accurate modelling of aeolian entrainment in thick atmospheres, such as those inferred for some extrasolar planets, our results also indicate that for environments with high density ratios, such as in jets on icy satellites or in tenuous atmospheres or exospheres, the correction for low-density-ratio conditions is not required.

Data from NASA's Cassini spacecraft show extensive linear dunes covering Titan's low latitudes^{1,2}. Unlike the silicate material that comprises most sand on terrestrial planets⁴, the dune sand on Titan is either organic or organic-coated water ice⁹, with likely densities of 0.4–1.5 g cm⁻³ (see discussion in ref. 10). In view of the deposition of organic aerosols from the atmosphere, the distinct compositions of dune and interdune surfaces suggest recent dune activity⁹. However, models of the present-day atmosphere give predominantly easterly (east-to-west) winds on the basis of conservation of angular momentum (see discussion in ref. 11), in contrast to the westerly (west-to-east) flow inferred from the streamlined appearance of dunes around topographic obstacles to the flow^{1,12}.

Knowledge of the threshold wind speed on Titan is fundamental to resolving this and other questions in Titan science. The dunes constitute one of the largest organic material reservoirs in the outer Solar System, and understanding how this material is mobilized across Titan depends on accurate understanding of threshold values. Knowledge of threshold wind speed is also necessary to model sand fluxes and dune migration rates¹³, as well as the relative effectiveness of competing resurfacing processes², including aeolian sedimentation and abrasion.

Threshold friction wind speed (u^*) is defined^{3,4} as a function of A , a dimensionless proportionality parameter dependent on both the particle Reynolds number at threshold friction wind speed ($Re^* = u^* D_p / \nu$; D_p , particle diameter; ν , kinematic viscosity) and the interparticle forces ($I_p \equiv I_p(D_p)$), and also as a function of particle, fluid and gravity characteristics:

$$u^*_{\text{t}} = A(Re^*_{\text{t}}, I_p) \sqrt{\frac{\rho_p - \rho}{\rho} g D_p} \approx A(Re^*_{\text{t}}, I_p) \sqrt{\frac{\rho_p}{\rho} g D_p} \quad (1)$$

Here ρ_p and ρ are respectively the particle and fluid densities and g is the acceleration due to gravity at the surface of Titan. Most of these functional parameters can be either set or derived in boundary-layer wind tunnels^{3,4} to quantify threshold wind speeds under a variety of boundary conditions. Compensation for functional parameters that cannot be set, for example g , is accomplished through data analysis and modelling. Experimental similitude parameters with values that approximate those of the natural setting ensure that atmospheric conditions are similar for the aeolian processes under investigation. Wind tunnel studies have yielded threshold wind speeds for particle motion on Earth, Mars and Venus⁴. For this work, we refurbished, and conducted experiments in, the high-pressure boundary-layer wind tunnel formerly used to simulate Venusian conditions⁵. The purpose was to simulate the conditions of aeolian saltation threshold on Titan. We refer to this facility as the Titan Wind Tunnel (TWT; Fig. 1 and Methods).

Previous publications have been equivocal in stating or suggesting the correct similitude parameter—kinematic viscosity^{14,15}, static pressure^{4,16,17} or density⁵—for saltation threshold experiments. We infer that the correct similitude parameter for determining threshold is kinematic viscosity, the ratio of molecular viscosity (μ) to fluid density (Methods). To match the kinematic viscosity of the surface atmosphere on Titan at terrestrial temperatures requires an absolute air pressure of $\sim 1.25 \times 10^6$ Pa (Extended Data Table 1). With this simulation, the fundamental physics governing particle threshold on Titan is reproduced. This physics is not achieved in wind tunnels designed to simulate conditions on Earth and Mars, and so model extrapolations to Titan conditions from experiments in those tunnels are questionable.

Our methodology for deriving threshold wind speeds on Titan (see Extended Data Fig. 1 for a flowchart) begins with the derivation of threshold friction wind speeds in the TWT (u^*_{tTWT}) for sediments of various sizes and densities (Methods and Extended Data Table 2). The experimentally derived values of u^*_{tTWT} were compared with predictions of the experimental conditions from two recognized models of threshold friction wind speeds, one model originally published by Iversen and White⁶ and the other by Shao and Lu⁷ (Methods). This comparison shows that the experimentally derived values are consistently ~ 40 – 50% higher, outside of uncertainty estimates, than predicted by either model (Extended Data Fig. 5; for calculation of uncertainty estimates, see Methods). These TWT threshold friction speeds were then converted to threshold friction speeds for the Titan surface (u^*_{tTitan}) for both models (Methods) and again compared with predictions from the two models (Fig. 2 and Table 1). We modified the Iversen–White model to give the interparticle force term the same dependence on D_p as in the Shao–Lu model (Methods), to facilitate comparison between the model results. The modified Iversen–White model underestimates the experimentally based values of u^*_{tTitan} by ~ 40 – 50% . The Shao–Lu model also

¹Earth and Planetary Sciences Department, University of Tennessee–Knoxville, 306 EPS Building, 1412 Circle Drive, Knoxville, Tennessee 37996, USA. ²Space Department, Johns Hopkins University Applied Physics Laboratory, Laurel, Maryland 20723, USA. ³SETI Institute, 189 Bernardo Avenue, Suite 100, Mountain View, California 94043, USA. ⁴Arizona State University, Tempe, Arizona 85287–1404, USA. ⁵Department of Mechanical Engineering, University of California Davis, California 95616, USA.

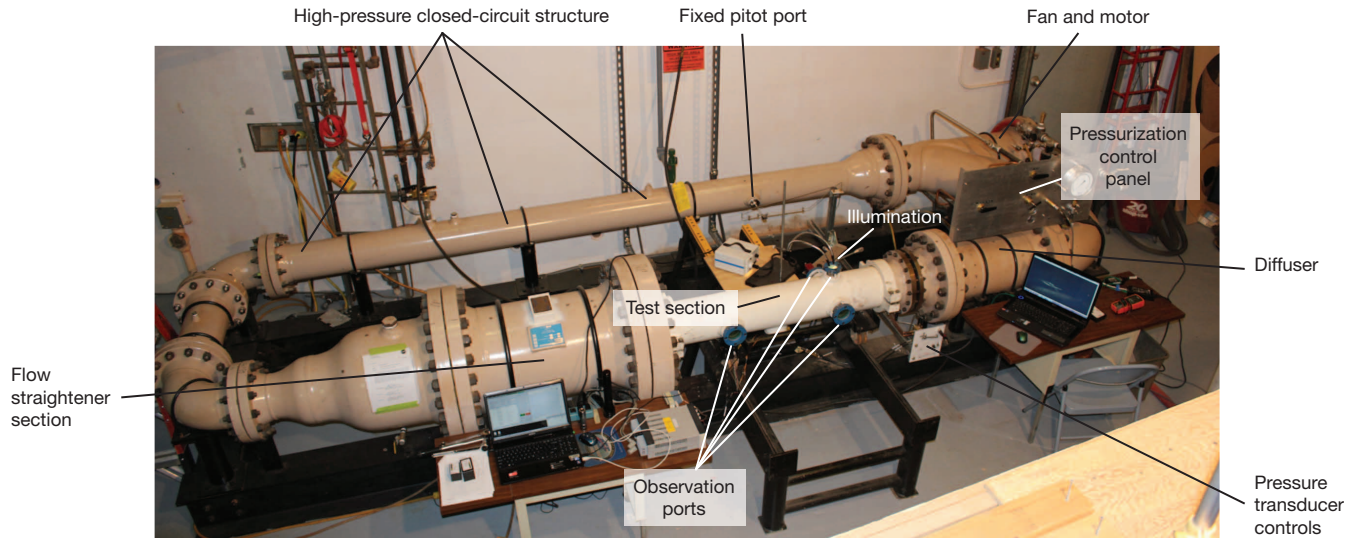


Figure 1 | Titan Wind Tunnel with important components labelled. The downwind observation side port through which the data of record are observed is the rightmost of the labelled observation ports.

underestimates the values by $\sim 40\text{--}50\%$ (Methods). Thus, the experimentally based threshold values for Titan conditions are higher than predicted by either model.

Correcting the models requires shifting the model curves to match the experimental results. Algebraic analyses of various model formulations^{6,8,18}

suggest the most reasonable approach to accomplishing this shift. As a specific form of equation (1), the complete formulation may be written

$$u^*_t = A_1 \sqrt{\left(\frac{1 + A_4 I_p / \rho_p g D_p^3}{f(\text{Re}^*_t) + g(\rho_p / \rho)} \right) \frac{\rho_p g D_p}{\rho}} \quad (2)$$

where A_4 is a constant that quantifies the interparticle force and $g(\rho_p / \rho)$ is a density ratio term (note the distinction between g and g). The value for A_4 in the various model formulations varied by roughly an order of magnitude (Extended Data Table 4) depending on whether the exponent for the particle diameter was fitted to the data or assumed, but this variation did not significantly change the magnitude of the curve. The Reynolds number dependence, $f(\text{Re}^*_t)$, has been derived on the basis of fitting to diverse data sets for discrete Reynolds number ranges^{4,6}, and so is unlikely to be significantly in error. A $\sim 40\text{--}50\%$ increase in the value of A_1 would correct the underestimation by the Iversen–White model, but the A_1 values have also been derived from fitting to a broad experimental data set, and a physical reason to change its value by $40\text{--}50\%$ is not obvious.

The magnitude of the modified Iversen–White model curve may also be increased through the inclusion of a density ratio term, $g(\rho_p / \rho)$. This term was introduced to improve the model fit to experimental data for Venus-analogue conditions, data that, like the TWT data, were higher in value than predicted⁸. The density ratios for the TWT experiments ($\sim 80\text{--}200$) and for Titan (~ 200) are similar to each other and to the value for the Venus-analogue experiments (~ 40), which (under density similitude) matches the value for Venus. In comparison, the density ratios for Earth and Mars are of orders 10^3 and 10^5 , respectively. Inclusion of the density ratio for Titan conditions shifts the modified Iversen–White model curve up, increasing the minimum $u^*_{t\text{Titan}}$ value by $\sim 50\%$, to a value approximately equal to that of the Shao–Lu model (Table 1). Inclusion of the density ratio term in the Shao–Lu model similarly shifts the corresponding curve up, although the model still underestimates the experimentally derived data, especially at large particle sizes (Fig. 2). The median value of the interparticle force coefficient suggested by Shao and Lu⁷ ($\gamma = 0.3 \text{ g s}^{-2}$) predicts a larger optimal particle diameter than is derived here, and so we use their minimum value of 0.1 g s^{-2} , shifting the optimal diameter to smaller sizes (Table 1). Whereas the Iversen–White model and the Shao–Lu model compare well for Earth and the various Martian conditions⁷, they show an observable difference for Venus⁷ and, with the modified Iversen–White model, an even greater difference ($\sim 100\%$ around a near-optimum D_p of $\sim 200 \mu\text{m}$) for Titan (Fig. 2). That both Venus and Titan have comparably lower

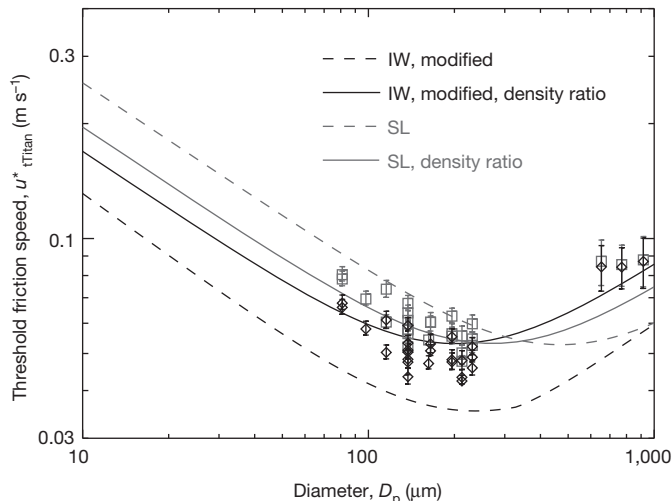


Figure 2 | Experimentally derived threshold friction wind speeds on Titan. The dashed lines are the nominal models by Iversen and White⁶ (IW) and by Shao and Lu⁷ (SL). The solid lines are the nominal models with the density ratio term⁸. For the nominal Iversen–White model, we use $K = 0.055 \text{ g s}^{-2}$, where K is equivalent to $A_4 I_p$ in the interparticle force term, and $n = 2$, where n is the exponent of D_p in the generalized interparticle force term (equation (6) in Methods, following ref. 8; Extended Data Table 4). This modification makes the interparticle force (I_p) proportional to D_p as in the Shao–Lu model, thereby facilitating comparison between the two models. The modified Iversen–White model (experimentally derived data in black symbols) is plotted for equations 5 ($0.03 \leq \text{Re}^*_p \leq 10$) and 6 ($10 \leq \text{Re}^*_p$) in ref. 6 (equations (7) and (8) in Methods), with the transition between the two particle friction Reynolds number regimes at $\sim 200 \mu\text{m}$. The Shao–Lu model (experimentally derived data in grey symbols) is plotted for equation 24 in ref. 7 (equation (9) in Methods) for the nominal value of A_N (0.0123), where A_N is the dimensionless proportionality parameter for the Shao–Lu model, and the lowest value for γ (0.1 g s^{-2}), where γ controls the interparticle force, as determined from optimizing the fit of the $u^*_{t\text{TWT}}$ data to the model (Extended Data Fig. 5). Vertical bars show standard deviation uncertainties in speed for the number of data points indicated in Extended Data Table 2; see Methods for the approach to calculating the uncertainty.

Table 1 | Comparison of u^*_{titan} values derived from both models

Value	Modified Iversen–White	Modified Iversen–White with density ratio	Iversen–White change	Shao–Lu	Shao–Lu with density ratio	Shao–Lu change
Minimum u^*_{titan} (m s^{-1})	0.035	0.053	~50% increase	0.053	0.053	None
Optimum D_p (μm)	236	206	~10% change	475	272	~40% decrease

In order to facilitate comparison between the two models, the Iversen–White model⁶ is modified to use the same dependence of interparticle force on D_p as in the Shao–Lu⁷ model (see Extended Data Table 4), using the formulation from refs 8, 18.

density ratios than both Earth and Mars substantiates the use of the density ratio to correct the Titan model curves.

The density ratio term was originally derived algebraically from a balance of forces for threshold conditions that include grain impacts⁸. However, the data of record in our TWT experiments were the observations made during increasing wind speeds, before significant upwind saltation began. Thus, they probably correspond to the fluid threshold, that is, the wind speed at which particles are first entrained by the fluid flow. By analogy with Titan (and Venus)¹⁹, the fluid threshold in the TWT (and Venus Wind Tunnel) experiments is lower than the impact threshold, that is, the lowest wind speed necessary to maintain saltation after initiation, and so would be encountered first as wind speed is increased. We thus infer that our experimental data, probably like those for the Venus Wind Tunnel⁵, record fluid thresholds without contributions from grain impacts. We infer A_1 to be a function of drag and moment¹⁸. That both A_1 and the density ratio term shift the Iversen–White model curve implies that a low density ratio affects the drag and moment in some fashion.

Our experimentally derived results provide parameters for improved modelling of sand transport on Titan. The threshold friction wind speeds (Fig. 2), translated into fluid shear stress ($\tau_t = \rho u^*_t{}^2$) (Fig. 3), provide values for numerical simulation of aeolian sediment flux. They can also be translated into threshold freestream wind speeds (no longer affected by surface friction) at specific elevations (Fig. 3) for use in atmospheric modelling or for comparison with model results. Greater threshold wind speeds increase the geomorphic effectiveness of winds that are strong enough to exceed threshold speeds, while eliminating the effect of weaker, although possibly more frequent, winds. Thus, the higher-than-predicted threshold wind speeds on Titan support a scenario in which only rare strong westerly winds, instead of prevailing easterlies, control the elongation of Titan dunes¹¹. However, our experimentally derived threshold values at an altitude of 300 m (Fig. 3) exceed the reported model threshold values at this height¹¹, and so use of the new threshold values in modelling dune elongation is necessary to test this hypothesis. Although the interparticle force is unknown on Titan, it is unlikely to be less than on Earth (Methods). If the dune sand on Titan is ‘sticky’²⁰, then the experimentally derived high threshold wind speeds would underestimate

the true threshold wind speeds, potentially further enhancing both the geomorphic effectiveness of stronger (westerly) winds and the difference between the experimentally derived and modelled threshold winds.

These results demonstrate the importance of including the density ratio term in calculating threshold friction speeds in thick atmospheres, as are likely to occur on some near-Earth-size extrasolar planets^{21,22}. Conversely, they help to substantiate its relative unimportance⁸ in modelling high-density-ratio conditions ($\rho_p/\rho > 1,000$). Thus, for other extreme aeolian conditions, including transport by plumes on Triton²³, jets on comets²⁴ or winds on Pluto, entrainment may be modelled by the modified Iversen–White^{6,8} formulation without the density ratio term. Under such low-gravity, low-sediment-density conditions, correct formulation of the interparticle force becomes especially significant. Whether either the modified Iversen–White model or the Shao–Lu model adequately represents the interparticle force term, given its complex dependence on particle characteristics²⁵, is a question for future research.

Online Content Methods, along with any additional Extended Data display items and Source Data, are available in the online version of the paper; references unique to these sections appear only in the online paper.

Received 7 April; accepted 17 November 2014.

Published online 8 December 2014.

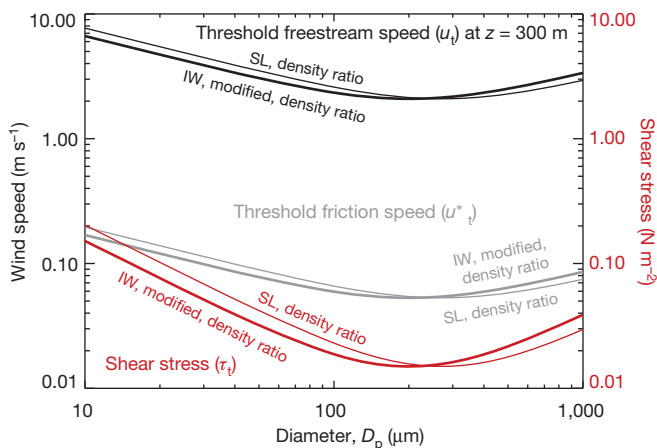


Figure 3 | Derived parameters from Titan threshold friction speeds. The u^*_{titan} data (grey lines) from Fig. 2 are presented as both shear stress values at threshold, $\tau_t = \rho u^*_t{}^2$ (red lines and right ordinal scale), and as freestream wind speed, $u(z)$, at $z = 300$ m altitude (black lines).

- Lorenz, R. D. *et al.* The sand seas of Titan: Cassini RADAR observations of longitudinal dunes. *Science* **312**, 724–727 (2006).
- Lopes, R. M. C. *et al.* Distribution and interplay of geologic processes on Titan from Cassini radar data. *Icarus* **205**, 540–558 (2010).
- Bagnold, R. A. *The Physics of Blown Sand and Desert Dunes* 1–106 (Methuen, 1941).
- Greeley, R. & Iversen, J. D. *Wind as a Geological Process: on Earth, Mars, Venus and Titan* Vol. 4, 67–106 (Cambridge Univ. Press, 1985).
- Greeley, R. *et al.* Windblown sand on Venus: preliminary results of laboratory simulations. *Icarus* **57**, 112–124 (1984).
- Iversen, J. D. & White, B. R. Saltation threshold on Earth, Mars and Venus. *Sedimentology* **29**, 111–119 (1982).
- Shao, Y. & Lu, H. A simple expression for wind erosion threshold friction velocity. *J. Geophys. Res.* **105**, 22437–22443 (2000).
- Iversen, J. D., Greeley, R., Marshall, J. R. & Pollack, J. B. Aeolian saltation threshold: the effect of density ratio. *Sedimentology* **34**, 699–706 (1987).
- Barnes, J. W. *et al.* Spectroscopy, morphometry, and photoclinometry of Titan's dune fields from Cassini/VIMS. *Icarus* **195**, 400–414 (2008).
- Burr, D. M., Emery, J. P., Lorenz, R. D., Collins, G. C. & Carling, P. A. Sediment transport by liquid surficial flow: application to Titan. *Icarus* **181**, 235–242 (2006).
- Tokano, T. Relevance of fast westerlies at equinox for the eastward elongation of Titan's dunes. *Aeolian Res.* **2**, 113–127 (2010).
- Lorenz, R. D. & Radebaugh, J. Global pattern of Titan's dunes: radar survey from the Cassini prime mission. *Geophys. Res. Lett.* **36**, L03202 (2009).
- White, B. R. Soil transport by winds on Mars. *J. Geophys. Res. Solid Earth* **84**, 4643–4651 (1979).
- Greeley, R., Iversen, J. D., Pollack, J. B., Udovich, N. & White, B. Wind tunnel studies of Martian aeolian processes. *Proc. R. Soc. Lond. A* **341**, 331–360 (1974).
- Iversen, J. D., Greeley, R., White, B. R. & Pollack, J. B. The effect of vertical distortion in the modeling of sedimentation phenomena - Martian crater wake streaks. *J. Geophys. Res.* **81**, 4846–4856 (1976).
- Greeley, R., Leach, R., White, B., Iversen, J. & Pollack, J. Mars - wind friction speeds for particle movement. *Geophys. Res. Lett.* **3**, 417–420 (1976).
- Greeley, R., Leach, R., White, B., Iversen, J. & Pollack, J. Threshold windspeeds for sand on Mars: wind tunnel simulations. *Geophys. Res. Lett.* **7**, 121–124 (1980).
- Iversen, J. D., Pollack, J. B., Greeley, R. & White, B. R. Saltation threshold on Mars: the effect of interparticle force, surface roughness, and low atmospheric density. *Icarus* **29**, 381–393 (1976).
- Kok, J. F., Parteli, E. J. R., Michaels, T. I. & Karam, D. B. The physics of wind-blown sand and dust. *Rep. Prog. Phys.* **75**, 106901 (2012).
- Rubin, D. M. & Hesp, P. A. Multiple origins of linear dunes on Earth and Titan. *Nature Geosci.* **2**, 653–658 (2009).
- Quintana, E. V. *et al.* An Earth-sized planet in the habitable zone of a cool star. *Science* **344**, 277–280 (2014).
- Charbonneau, D. *et al.* A super-Earth transiting a nearby low-mass star. *Nature* **462**, 891–894 (2009).

23. Sagan, C. & Chyba, C. Triton's streaks as windblown dust. *Nature* **346**, 546–548 (1990).
24. Cheng, A. F., Lisse, C. M. & A'Hearn, M. Surface geomorphology of Jupiter family comets: a geologic process perspective. *Icarus* **222**, 808–817 (2013).
25. Jones, R., Pollock, H. M., Cleaver, J. A. S. & Hodges, C. S. Adhesion forces between glass and silicon surfaces in air studied by AFM: effects of relative humidity, particle size, roughness, and surface treatment. *Langmuir* **18**, 8045–8055 (2002).

Acknowledgements This research was supported by grants from NASA's Planetary Geology and Geophysics Program and the Outer Planets Research Program. We dedicate this manuscript to our colleague R. Greeley, who was the motivating force behind the construction of the Planetary Aeolian Laboratory at the NASA Ames Research Center and used it over several decades to make fundamental and long-lasting contributions to understanding aeolian processes on other bodies.

Author Contributions D.M.B. is the principal investigator on the NASA grants that funded this work. She conceived the work, defined the objectives, oversaw the wind

tunnel refurbishment, oversaw and participated in the data collection, analysis and reduction, and led the writing of the manuscript. N.T.B. contributed fundamental ideas and calculations during wind tunnel refurbishment, participated in the data collection, analysis and reduction, and contributed to writing the manuscript. The Titan Wind Tunnel is housed in the Planetary Aeolian Laboratory at the NASA Ames Research Center. J.R.M. and J.K.S. provided practical assistance, in conjunction with NASA personnel, to complete the wind tunnel refurbishment and calibration. J.K.S., the engineer at the Planetary Aeolian Laboratory, provided sieved sediments for the experiments, maintained and operated the wind tunnel during all runs, and provided data logs from all runs. B.R.W. contributed ideas during project design, wind tunnel refurbishment and data collection. J.P.E. provided assistance in data reduction and analysis, and contributed to writing the manuscript.

Author Information Reprints and permissions information is available at www.nature.com/reprints. The authors declare no competing financial interests. Readers are welcome to comment on the online version of the paper. Correspondence and requests for materials should be addressed to D.M.B. (dburr1@utk.edu).

METHODS

Titan Wind Tunnel. The TWT (Fig. 1), a remodel of the Venus Wind Tunnel^{5,26}, is a closed-circuit, high-pressure, boundary-layer tunnel. Flow is generated by an eight-bladed fan rotating at a rate of up to 2,500 r.p.m. Downwind of the fan, ten curved tubes, each 5 cm in diameter, prevent flow separation and minimize turbulence and secondary flow. Downwind of these flow straighteners, a settling chamber further damps turbulence and traps material before entering the test section. In the test section, at pressures necessary to simulate Titan kinematic viscosity at standard temperature (12 bar; Extended Data Table 1), the fan drives air flow at freestream speeds ($u(z)$) of up to $\sim 6.5 \text{ m s}^{-1}$. Downwind of the test section, a diffuser expansion section prevents material from recirculating with the gas flow and impinging on the fan or plugging the fixed pitot tube, located downwind of the fan.

The test section is 122 cm in length and 20.3 cm in interior diameter, and moves laterally on rails into or out of its position within the wind tunnel. Floor plates—either the calibration plate with a traversable pitot tube or the experimental test plate with no pitot tube—have the same length as the test section and are 18 cm in width. When inserted into the test section (Extended Data Figs 2 and 3), they rest against the inside walls. The test section has two stations for observing the test bed: a single upwind observation port 30 cm from the upwind end of the test section, and three downwind observation ports, including two ports on either side of the test section identical to the upwind port and a smaller port on top to enable illumination of the test bed.

The TWT operates with pressurized air that is desiccated by an Airtek TW250 dryer to dew point of -40°C . Temperature variations are negligible given the large fluid mass within the tunnel. Static pressure is monitored visually using a calibrated gauge.

The TWT is fitted with a custom-made, high-pressure, high-temporal-resolution transducer supplied by the Tavis Corporation. Wind speed data, both for calibrations and threshold wind speed information, were collected using pitot tubes (see, for example, Extended Data Fig. 3b) connected to this transducer. Pneumatic lines from the pitot tube exit from beneath the plate to a signal pass-through port in the bottom of the test section. The electrical lines that supply power and control to the instrument and enable data capture are run to a laptop computer through the same pass-through. The pneumatic lines run through the stack valve to the dynamic pressure transducer. Transducer output consists of voltage as a function of dynamic pressure according to manufacturer-supplied calibration curves. These dynamic pressures, in turn, are converted to freestream wind speeds at height z as

$$u(z) = (2P_{\text{dyn}}/\rho)^{1/2} \quad (3)$$

where P_{dyn} is the dynamic pressure of the gas (air) and is a function of z ($P_{\text{dyn}} = P_{\text{dyn}}(z)$).

TWT calibration. Derivation of threshold friction wind speeds in the TWT entailed initial collection of wind tunnel calibration data (Extended Data Fig. 4). Different types of calibration data were required.

(i) Although wind speed (dynamic pressure) data were required in the test section, where threshold was observed, the traversable pitot tube in the test section had to be removed during experiments to prevent clogging or disruption of air flow. Dynamic pressure data were collected instead using the fixed pitot tube on the opposite side of the wind tunnel (Fig. 1). Thus, a correlation curve was derived to convert the freestream wind speed data collected during experiments with the fixed pitot tube into equivalent freestream wind speed data in the test section. We constructed this curve from three separate calibration runs (interspersed with threshold data collection runs) at fan motor speeds up to 105% of maximum rated speed in 20% increments. During these runs, voltage data from the transducer were collected independently and alternately from the traversable pitot tube and from the fixed pitot tube by switching the stack valve to read either the fixed pitot or traversable pitot for the same fan motor speed increment. Those voltage data were converted to dynamic pressures using the manufacturer's curves and then from dynamic pressures into freestream wind speeds using equation (3). The resultant correction curve is $u(z)_{\text{TWT}} = 1.49u(z)_{\text{fixed pitot}} - 0.426$, where $u(z)_{\text{fixed pitot}}$ is the freestream wind speed at the fixed pitot and $u(z)_{\text{TWT}}$ is the freestream wind speed in the test section. Both the fixed pitot and (during this calibration) the traverse pitot in the test section are within the boundary layer, and so record freestream wind speeds.

(ii) Freestream wind speed at height z , $u(z)$, is related to friction wind speed, u^* , according to the 'law of the wall',

$$u(z) = (u^*/\kappa)\ln(z/z_0) \quad (4)$$

where κ is the von Kármán constant (0.41) and z_0 is the roughness height, that is, the distance above the surface at which the wind speed is zero. Thus, to convert the freestream wind speeds at threshold ($u(z)_t$) into the desired friction wind speeds at

threshold (u^*_t) requires knowledge of the roughness height. Equation (4) can be linearized to

$$\ln(z) = (\kappa/u^*)u(z) + \ln(z_0) \quad (5)$$

In aeolian studies, this roughness height is commonly derived by measuring a wind speed profile to construct the relationship between height and freestream wind speed³. As indicated by equation (5), the y intercept of a plot of $\ln(z)$ versus $u(z)$ is $\ln(z_0)$, such that the value of $e^{(y\text{intercept})}$ gives the roughness height.

To derive the roughness height, we performed a series of calibration runs to determine the boundary-layer profiles. A calibration plate of aluminium was covered with 100-grit sand paper (grain diameters of 125 μm), and a traversable pitot tube assembly with a stepping motor assembly was installed at the downwind end of the plate (Extended Data Fig. 3b). The stepping motor raised the pitot tube in logarithmically increasing steps above the plate to a maximum height of $\sim 4.3 \text{ cm}$, well into the freestream (Extended Data Fig. 4). At each step, the dynamic pressure from the pitot tube was read over a 10 s interval by the transducer. The voltage from the transducer was sent to a data acquisition module manufactured by Measurement Computing Corporation, and was processed and recorded by TracerDAQ software on a laptop computer. After data collection, voltages were converted to dynamic pressures using the appropriate pressure-dependent correlation curve provided by the transducer manufacturer (Tavis Corporation), and these dynamic pressures were in turn converted to freestream wind speeds using equation (3). These boundary-layer data taken at different wind speeds show that the freestream boundary layer begins at $z \approx 1.9 \text{ cm}$, such that the pitot tube reached well into the freestream and the boundary layer was fully developed, and that $z_0 \approx 0.003 \text{ cm}$ (Extended Data Fig. 4).

These calibration runs were conducted at fan motor speeds of 20% to 80% of the maximum rated speed, increasing in 10% increments. We used the average value of these multiple calibration runs. The same data are also used to derive u^* , which is used in uncertainty estimates (see below).

Kinematic viscosity as similitude parameter for threshold experiments. Kinematic viscosity (ν), is the ratio of molecular viscosity (μ) to fluid density (ρ). For a particle of a given diameter, kinematic viscosity is a fundamental control on the relative importance of lift and drag forces, which is quantified by the particle friction Reynolds number:

$$\text{Re}^*_p = u^*D_p/\nu = u^*D_p\rho/\mu$$

Here D_p is the particle diameter and u^* is the friction wind speed. The particle friction Reynolds number is a controlling parameter in the formulation for threshold friction wind speed (equation (1)). For smaller particles, threshold is controlled largely by the viscous (or laminar) sublayer, of thickness δ_v , within which the flow regime is linear and the mechanics of particle detachment differ from those in the turbulent regime¹⁹. The thickness of this viscous sublayer is proportional to the kinematic viscosity and inversely proportional to the friction speed:

$$\delta_v \approx 5\nu/u^* \approx 5\mu/\rho u^*$$

Thus, correctly simulating the kinematic viscosity is necessary in deriving threshold friction wind speeds, providing the correct ratio of lift and drag forces, and simulating the viscous sublayer thicknesses.

Selection and preparation of experimental sediments. The experimental sediments were chosen to encompass a range of densities, median particle diameters (D_p) and particle diameter ranges (Extended Data Table 2). This distribution includes sediments believed to be similar in size to the sand on Titan and of equivalent weight for both organic and water ice compositions. In addition, the experimental matrix includes several sediments of both larger and smaller grain sizes and various densities, to give more complete coverage of the wind-speed/particle-diameter space for more robust comparison with threshold models.

After sieving, the experimental sediments were added to the test plate within the test section and smoothed to ensure complete coverage with a consistent thickness ($\sim 1 \text{ cm}$) (Extended Data Fig. 2). The test section was rolled back into alignment with the tunnel, which was sealed and pressurized with dry air (dew point at -40°C).

Relative interparticle forces of experimental and Titan conditions. We set conditions in the TWT to mimic cohesive forces expected for Titan. The largest contributor to interparticle force on Earth (that is, humidity) is due to the polarity of water molecules, but water vapour and other polar molecules are lacking in Titan's atmosphere. Thus, the experimental sediments in the TWT are dry, as noted above, so that cohesive forces due to the polarity of the water molecules are negligible, as is the case for sediments on Titan. The values for interparticle force in the threshold models that were fitted to the TWT data can be computed as the product of the interparticle force term (Extended Data Table 4) and a representative grain diameter, taken to be $\sim 200 \mu\text{m}$, the approximate optimal particle size for saltation on Titan (Fig. 2). In the modified Iversen–White model, the interparticle force at that particle size is $\sim 11 \text{ nN}$, and for the Shao–Lu model the value is $\sim 20 \text{ nN}$. For comparison,

atomic force microscopy experiments derive pull-off forces for $\sim 200 \mu\text{m}$ -diameter hydrophobic particles under dry conditions of ~ 10 to 500 nN (refs 25, 27). Calculation of interparticle force for 'clean' particles of that diameter using relationships derived from lunar soils²⁸ suggests even higher values, of $\sim 3,600 \text{ nN}$. On terrestrial bodies, sediment cohesion may be enhanced by electrostatic forces generated by friction between both rocky and icy (snow) particles²⁹, and the blown sands on Titan, being composed of organic compounds or water ice (or both), probably experience similar electrostatic forces. Other processes, such as wetting by liquid hydrocarbons, may enhance these high cohesion values even further. Thus, it is unlikely that the cohesive forces on Titan will be less strong than in these wind tunnel experiments. Therefore, the threshold wind speed models derived from these experiments probably represent minimum values, exacerbating the mismatch between the data and the models. The morphology of the dunes, which could be interpreted as evidence for unusually high sand cohesion²⁰, provides some supporting evidence for high cohesive forces on Titan. Further work is required to quantify the magnitude of interparticle forces for wind-blown sediments on any planetary body^{19,29}.

Collection of threshold wind speed data. Following established procedures^{5,16,18}, we momentarily increased the wind speed until motion was briefly observed, to remove perched grains or otherwise easily moved grains from the bed, thereby making the surface similar to that expected to exist at equilibrium in an aeolian environment. Threshold wind speed data were then collected by observation of motion in the test section. Our interest is in the fluid (or static) threshold, the wind speed at which particles are first entrained by the fluid flow, as distinct from impact threshold, the lowest wind speed necessary to maintain saltation after initiation. For these fluid threshold data, fan motor speed was gradually increased while visual observations were made of five stages of grain motion, namely first motion, flurries, patches, motion of $\sim 50\%$ of the longitudinally central portion of the bed, and motion of $\sim 100\%$ of the bed (Extended Data Table 3). The fan motor speed was then decreased as similar stages were noted in reverse.

We define threshold as 50% of the bed in motion, indicating that one-half of the grains have exceeded threshold and the other half have not. We focus on the longitudinally central portion of the bed to avoid effects along the walls. Early work defined threshold as "the lowest ... speed at which the majority of exposed particles ... are set in motion" and "general motion of the exposed particles"¹⁸ or "movement of particles over the entire bed"¹⁶, consistent with ref. 3. If 'general motion' indicates that the entire bed is in motion, our definition of 50% of the bed in motion is equally or more conservative—tending towards lower wind speeds—than the definitions in these references. Later work by some of the same authors defined threshold as the wind speed at which "groups of grains began to saltate" such that "at slightly higher wind speeds, saltation was a continuous cloud of particles"⁵. In our observations, motion of 50% of the bed occurred as groups of saltating grains and immediately preceded continuous saltation over the entire bed. Thus, our definition of threshold seems qualitatively consistent with this definition as well. Because of our focus on fluid threshold, we use the value for motion of 50% of the bed during increasing wind speeds.

Observations of grain motion were made by two independent observers at both the upwind and downwind viewing ports to provide confirmation of motion. The observations from the downwind port are considered the threshold data of record because the $\sim 80 \text{ cm}$ fetch allows for development of the turbulent boundary layer and for any anomalous effects from the leading edge of the test plate to damp out. The observations focused on roughly the central third of the bed along its horizontal axis (that is, perpendicular to the wind stream) within the field of view to avoid anomalous conditions associated with the side walls of the test section.

Voltages from a high-precision, high-pressure transducer connected to the fixed pitot tube in the freestream were continuously recorded throughout each experiment. As each grain motion stage was observed in the test section, the time and fan motor speed were noted. Data on grain motion stages were collected during three successive runs from the same bed of material and showed excellent reproducibility.

The continuous voltage data were then converted to threshold friction wind speeds in the test section. This conversion entailed first using the manufacturer-supplied calibration curves of transducer voltage versus applied pressure to derive the dynamic pressure. These dynamic pressures were then converted to freestream wind speeds (using equation (3)), effectively creating a look-up table of wind speed by time. The recorded times for each grain motion stage were used to query this look-up table to find the wind speeds at each grain motion stage, including threshold. The correlation curve to convert freestream wind speeds derived from the fixed pitot tube into equivalent freestream wind speeds in the test section was then applied (see Fig. 1 for pitot tube locations). Finally, these threshold freestream wind speeds were translated into threshold friction wind speeds, u^*_{TWT} , according to the 'law of the wall', (equation (4), in which z , the freestream wind speed height, is derived from appropriate boundary layer curves (Extended Data Fig. 4)).

Models used for comparison of TWT threshold friction wind speeds. Model of Iversen and White. This model^{4,6} is based on mathematically fitting data from

terrestrial and low-pressure planetary-analogue wind tunnel experiments. The form of the model is

$$u^*_{\text{t}} = A_1 f(\text{Re}^*_t) \left([1 + K/(\rho_p g D_p^n)] (\rho_p/\rho) g D_p \right)^{1/2} \quad (6)$$

where $u^*_{\text{t}} = A_1 f(\rho_p/\rho) g D_p^{1/2}$ is the original equation (derived in ref. 3). Comparison with equation (1) shows that $A = A_1 f(\text{Re}^*_t)$ and that the term $(1 + K/(\rho_p g D_p^n))^{1/2}$, in which $K = 0.006 \text{ g cm}^{0.5} \text{ s}^{-2}$ and $n = 2.5$, is an expression for the importance of interparticle forces relative to gravity. However, previous¹⁸ and subsequent iterations⁸ of this model used an a priori proportionality of I_p to D_p ($n = 2$), for which the (fitted) value of K is 0.055 g s^{-2} (Extended Data Table 4). In this work, we modify the Iversen–White model by using $K = 0.055 \text{ g s}^{-2}$ and $n = 2$ (after ref. 8) to facilitate its comparison with the Shao–Lu model⁷.

Model of Shao and Lu. This model⁷ is a deliberate simplification of the Iversen–White model^{4,6}, replacing the modest dependence of A on Reynolds number with a constant. Unlike Iversen and White^{4,6} but consistent with the previous¹⁸ and subsequent⁸ iterations of the Iversen–White model, the Shao–Lu model sets I_p proportional to D_p .

Conversion to threshold friction wind speed on Titan. The TWT simulates the kinematic viscosity of flow around the grains but not the atmospheric density, the gravity of Titan nor the variation in A , as required in the model of Iversen and colleagues^{6,8,18} (formulated in equations (1) and (2)). On the basis of equation (1), conversion of the threshold friction speed from the wind tunnel, u^*_{TWT} , to the threshold friction speed on the surface of Titan, u^*_{Titan} , may be implemented as:

$$u^*_{\text{Titan}} = u^*_{\text{TWT}} (A_{\text{Titan}}/A_{\text{TWT}}) [(g_{\text{Titan}}/g_{\text{TWT}}) (\rho_{\text{TWT}}/\rho_{\text{Titan}})]^{1/2}$$

Although the direct correction for gravity and particle density is trivial, correcting for A (which depends also on the particle Reynolds number and the particle size) is more complex. Our approach was to compute theoretical values of u^*_{Titan} and u^*_{TWT} as functions of particle size using the appropriate expression for A and corresponding parameters^{4,6}. We then multiplied the u^*_{TWT} values (Extended Data Fig. 5) by the ratio $(u^*_{\text{Titan}}/u^*_{\text{TWT}})_{\text{theoretical}}$ (Extended Data Fig. 6) to translate these experimentally derived wind speeds to Titan surface conditions (u^*_{Titan}), using a density for Titan sediment of 1 g cm^{-3} .

Comparison of u^*_{Titan} with models. Model of Iversen and White⁶. For the modified Iversen–White model, we use $K = 0.055 \text{ g s}^{-2}$ and $n = 2$ (following ref. 8). This modification to the Iversen–White model gives the same dependence of interparticle force (I_p) on D_p as the Shao–Lu model, thereby facilitating comparison between the two models. For this model, u^*_{Titan} was found by first determining the Reynolds number range ($\text{Re}^*_t \geq 3$) for the relevant particle sizes ($10 \mu\text{m} \leq D_p \leq 1,000 \mu\text{m}$) and flow speeds on Titan. For this range of particle Reynolds number, both expressions for A from the Iversen–White model are used. These expressions are

$$A = 0.129 \left(1 + \frac{0.055}{\rho_p g D_p^2} \right)^{1/2} (1.928 \text{Re}^*_t^{0.092} - 1)^{1/2} \quad (7)$$

for $3 \leq \text{Re}^*_t \leq 10$ and

$$A = 0.120 \left(1 + \frac{0.055}{\rho_p g D_p^2} \right)^{1/2} \left(1 - 0.0858 e^{[-0.0617(\text{Re}^*_t - 10)]} \right) \quad (8)$$

for $\text{Re}^*_t \geq 10$ (refs 4, 6). From equations (1), (7) and (8), we calculated values of u^*_{TWT} and u^*_{Titan} for the actual values of D_p used in our experiments, calculated the ratio of u^*_{Titan} to u^*_{TWT} as a function of grain size (Extended Data Fig. 6), and multiplied these ratios by u^*_{TWT} to get u^*_{Titan} as a function of grain size.

Model of Shao and Lu⁷. The Shao–Lu model assumes that the coefficient A is only weakly dependent on the particle friction Reynolds number. In addition, aerodynamic drag and lift are balanced by cohesion and gravity (both functions of grain size), so that the threshold is dependent only on grain size. Thus, A is reduced to a constant (A_N) and the remainder of the expression may be expressed as a function of particle size with an empirical constant (γ) for interparticle forces, as follows:

$$u^*_{\text{t}} = (A_N [(\rho_p/\rho) g D_p + \gamma/(\rho D_p)])^{1/2} \quad (9)$$

Here A_N has a value of approximately 0.0123 and γ is approximately 0.3 g s^{-2} .

For the Shao–Lu model, like the Iversen–White model, conversion of u^*_{TWT} to u^*_{Titan} entailed multiplying by $(u^*_{\text{Titan}}/u^*_{\text{TWT}})_{\text{theoretical}}$ (Extended Data Fig. 6) and using the given value of A_N (0.0123) and the lowest value within the indicated range of values for γ (0.1 g s^{-2}) as derived for the TWT data (Extended Data Fig. 5). Lower γ values effectively decrease the interparticle force, causing the transition between dominance by interparticle forces and dominance by gravity to shift to smaller grain sizes. This shift leaves the curve unchanged at the largest particle diameters and moves it down at smaller particle diameters. With this shift, the nominal Shao–Lu model underestimates u^*_{Titan} by 40 – 50% at all particle diameters. Lower

values of γ are outside the range indicated by Shao and Lu⁷ on the basis of data on terrestrial planets.

Uncertainty estimates. We calculate uncertainties in our results for the TWT (Extended Data Fig. 5) as explained below. In this explanation, we provide example values for one sediment type, 175–250 μm silica sand (see, for example, Extended Data Fig. 2). Data for this sediment were collected on three runs (T-13-135, T-13-136 and T-13-137). Threshold (50% of the bed in motion) was not observed during T-13-136. That is, as fan motor speed was increased during the experiments, we were not always able to identify accurately or quickly enough when the bed transitioned from less than 50% of the bed in motion ('patches'; see Extended Data Table 3) to more than 50% of the bed in motion. Such non-identifications, as for T-13-136, reduced the number of data points for any series of three or four runs per sediment type.

A. Voltage as measured at the fixed pitot at threshold. The uncertainty in the voltage recorded at the time that threshold is observed is due to two factors.

- Transducer uncertainty. We quantify this fractional uncertainty as the ratio of the 'Deviation (mV)' and the 'Output Voltage (VDC)' (VDC, d.c. voltage in volts) recorded in the manufacturer's transducer calibration data. The maximum fractional uncertainty over the entire range of test pressures is always $\leq 1\%$. 1% is taken as a standard, conservative value.

- Voltage variability. The fractional uncertainty in the voltage variability is the standard deviation of the population divided by the average voltage. This uncertainty is calculated for the ten seconds after threshold is observed. For T-13-135, the average voltage is -0.73 VDC, the standard deviation is 0.019 VDC and the fractional uncertainty is 0.024 or 2.4% . For T-13-137, the average voltage is -0.77 VDC, the standard deviation is 0.019 VDC and the fractional uncertainty is 0.027 or 2.7% .

Because these uncertainties in the voltage at threshold are random and independent, they are added in quadrature. For the two runs of 175–250 μm silica sand for which threshold was observed, the results are 2.6% and 2.9% .

B. Conversion from fixed pitot voltages to pressures. Conversion from voltage to dynamic pressure is done using the manufacturer-supplied linear calibration curves, for which the uncertainty is $<0.01\%$. Given the linear shape of the curves and their small uncertainty, we consider this uncertainty to be negligible.

C. Conversion from fixed pitot pressures to fixed pitot freestream wind speeds. Dynamic pressure from the fixed pitot tube as recorded by the transducer is converted to wind speed according to equation (3), where ρ is calculated using the universal gas law (as indicated in Extended Data Table 1). The static pressure (P) for this calculation is measured with a precision of $<0.5\%$ using a calibrated gauge. The temperature in the wind tunnel is taken as the temperature in the room (the Planetary Aeolian Laboratory), which is measured with a calibrated thermometer. Thus, the fractional uncertainty in density ($\delta\rho/\rho$) is the fractional uncertainty in the static pressure ($\delta P/P$), and is taken to be 0.5% .

The fractional uncertainty in the wind speed ($\delta u/u$) at the fixed pitot is derived by propagating uncertainties in the dynamic pressure (P_{dyn}) and the density (ρ):

$$\delta u/u = (1/2)[(2\delta P_{\text{dyn}}/P_{\text{dyn}}) + \delta\rho/\rho]$$

To average these uncertainties for the two runs for 175–250 μm silica sand which threshold was observed, the fractional uncertainties in wind speed were converted into absolute uncertainties, added in quadrature and converted back to fractional uncertainties. For 175–250 μm silica sand, the result is 3.7% .

D. Conversion of fixed pitot freestream wind speeds to equivalent freestream wind speed in the test section. The freestream wind speeds at the fixed pitot tube are converted to equivalent freestream wind speeds in the test section using an average correlation curve. This correlation curve was derived from data collected during three calibration runs interspersed with data collection runs. The data used in the curve were those at which threshold was observed ($\sim 1\text{--}2\text{ m s}^{-1}$). The fractional

uncertainty in the correlation curves derived from these three runs is used as the uncertainty in this correlation. This fractional uncertainty is estimated to be the ratio of the standard deviation of the population and the average wind speed. For threshold speeds of $1\text{--}2\text{ m s}^{-1}$, the result ranges from 1.5% to 0.3% . 1.5% is used as a standard, conservative value.

The uncertainties in these two conversions above are independent and so are added in quadrature. For 175–250 μm silica sand, the result is 4.0% .

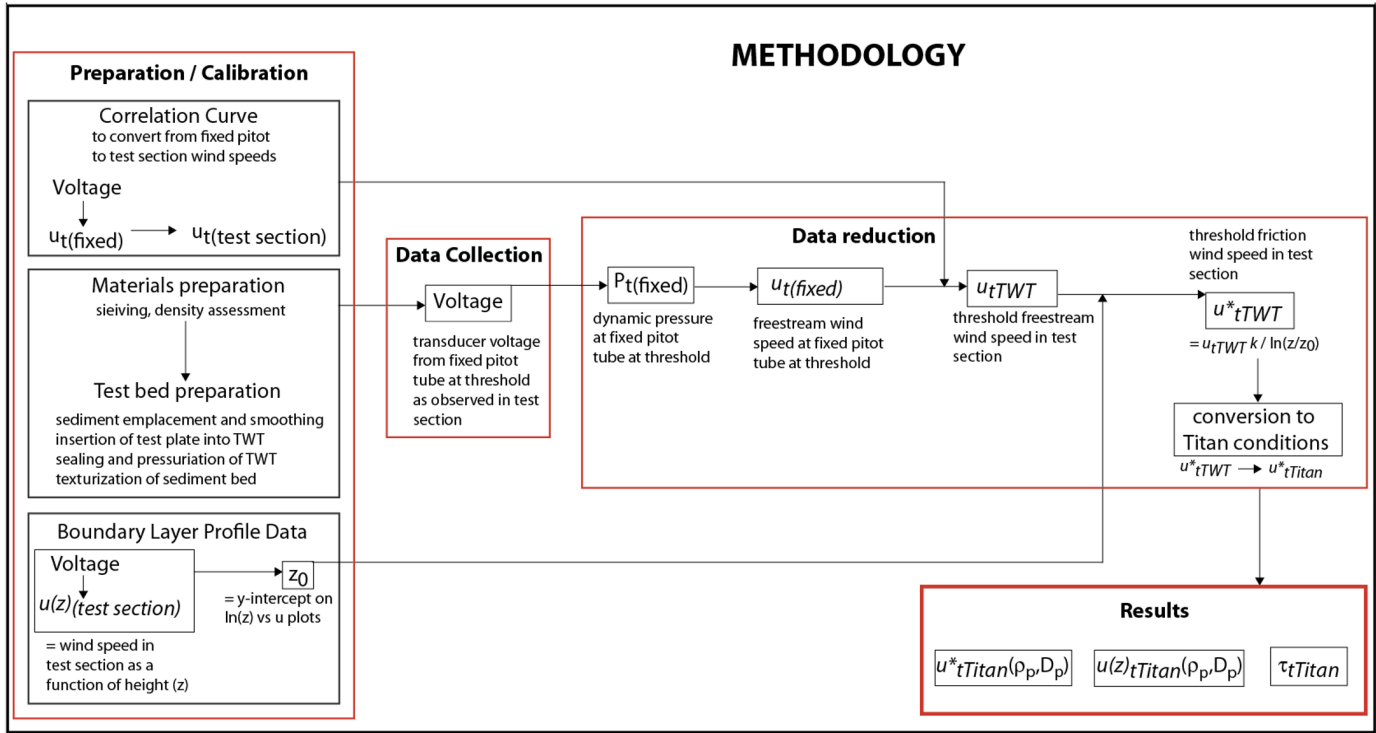
E. Determination of observational uncertainty in the freestream wind speed. Threshold is determined to occur in the wind tunnel by visual observation of 50% bed motion. Three or four experiments were run for each sediment type (unique combination of material and size). For each sediment type, the variability of the wind speed at which threshold was observed is quantified as the standard deviation of the population, which was divided by the threshold wind speeds to yield fractional uncertainty. For three sediment types, threshold was observed during only one run, and so a standard deviation could not be calculated. Without the standard deviation, the uncertainties depicted in Extended Data Figs 5 for these three (out of 27) data points slightly underestimate the true uncertainties. For silica sand (runs T-13-135 and T-13-137), the standard deviation of the population is 0.030 m s^{-1} , corresponding to a fractional uncertainty of 2.2% .

F. Conversion of freestream wind speed in the test section to TWT friction wind speed. The freestream wind speeds are converted into friction wind speeds using the 'law of the wall' (equation (4)). The uncertainty in this conversion derives from uncertainty in the roughness height. We used the value of z_0 derived from the calibration runs for the wind speeds at which threshold was observed ($20\%\text{--}30\%$ of the maximum rated fan motor speed). These values can be checked against theoretical values for z_0 . For a roughness Reynolds number (Re_τ) >60 , $z_0 = k_s/30$, where k_s is the Nikuradse roughness; roughness in the transitional regime down to $\text{Re}_\tau = 4$ is similar to roughness in the aerodynamically rough regime, and so the same formulation is commonly used¹⁹. In the aerodynamically smooth regime where $\text{Re}_\tau < 4$, $z_0 = \mu/9\rho u^*$. To capture the variability in z_0 , we averaged six different values: the roughness heights at 20% , 30% , 40% , 50% , 60% and 80% of the maximum rated fan motor speed (see, for example, Extended Data Fig. 4). The uncertainty in z_0 was characterized as the standard deviation of these values. That absolute uncertainty, $\sim 0.0016\text{ mm}$, was both added and subtracted from the average z_0 to get absolute positive and negative uncertainties, which were then converted to fractional uncertainties. Adding these uncertainties in quadrature with the previous uncertainties from step E gave the final fractional uncertainties for each sediment type. For silica sand, the TWT fractional uncertainties are 5.4% (run T-13-135) and 4.8% (run T-13-137).

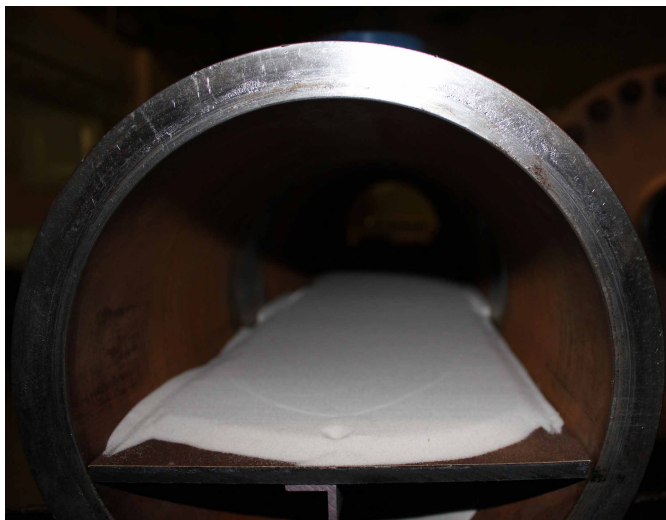
G. Conversion of TWT friction wind speed to Titan friction wind speed. The TWT friction wind speeds were converted to Titan friction wind speeds through scaling by the ratio of the TWT threshold friction speeds and the Titan threshold friction wind speeds. For silica sand (runs T-13-135 and T-13-137), this ratio is 0.4796 . Because this step consists of multiplication by a constant, the fractional uncertainties do not change. For plotting in Fig. 2, all the values for each sediment type and grain size were averaged together.

The results of this error analysis are shown in Extended Data Table 2.

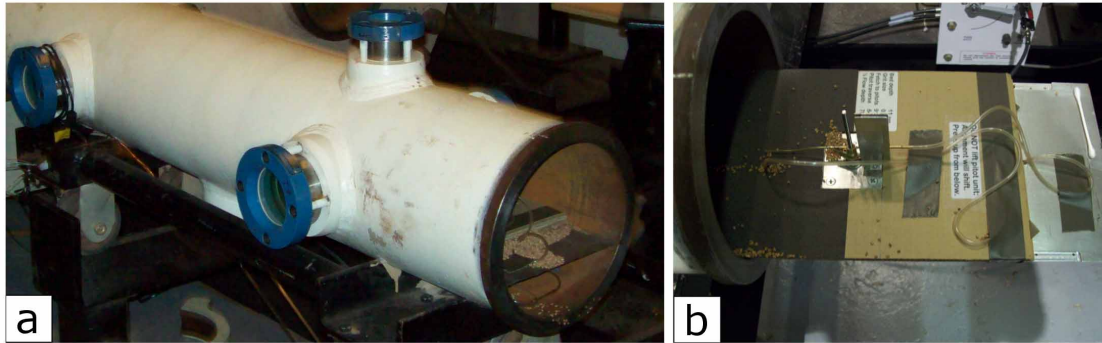
- Marshall, J. R. & Greeley, R. An experimental study of aeolian structures on Venus. *J. Geophys. Res. Planets* **97**, 1007–1016 (1992).
- Hodges, C. S., Cleaver, J. A. S., Ghadiri, M., Jones, R. & Pollock, H. M. Forces between polystyrene particles in water using the AFM: pull-off force vs particle size. *Langmuir* **18**, 5741–5748 (2002).
- Scheeres, D. J., Hartzell, C. M., Sánchez, P. & Swift, M. Scaling forces to asteroid surfaces: the role of cohesion. *Icarus* **210**, 968–984 (2010).
- Merrison, J. P. Sand transport, erosion and granular electrification. *Aeolian Res.* **4**, 1–16 (2012).



Extended Data Figure 1 | Flow chart of methodology showing the steps used in this work. The results are threshold friction wind speed on Titan, u_{tTitan}^* , and freestream wind speed at height z , $u(z)_{tTitan}$, as a function of particle density (ρ_p) and diameter (D_p), and the shear stress at the surface at threshold (τ_{tTitan}). Upright font denotes calibration data or informational text. Italic font indicates measured wind speeds or parameters derived from measured wind speeds.

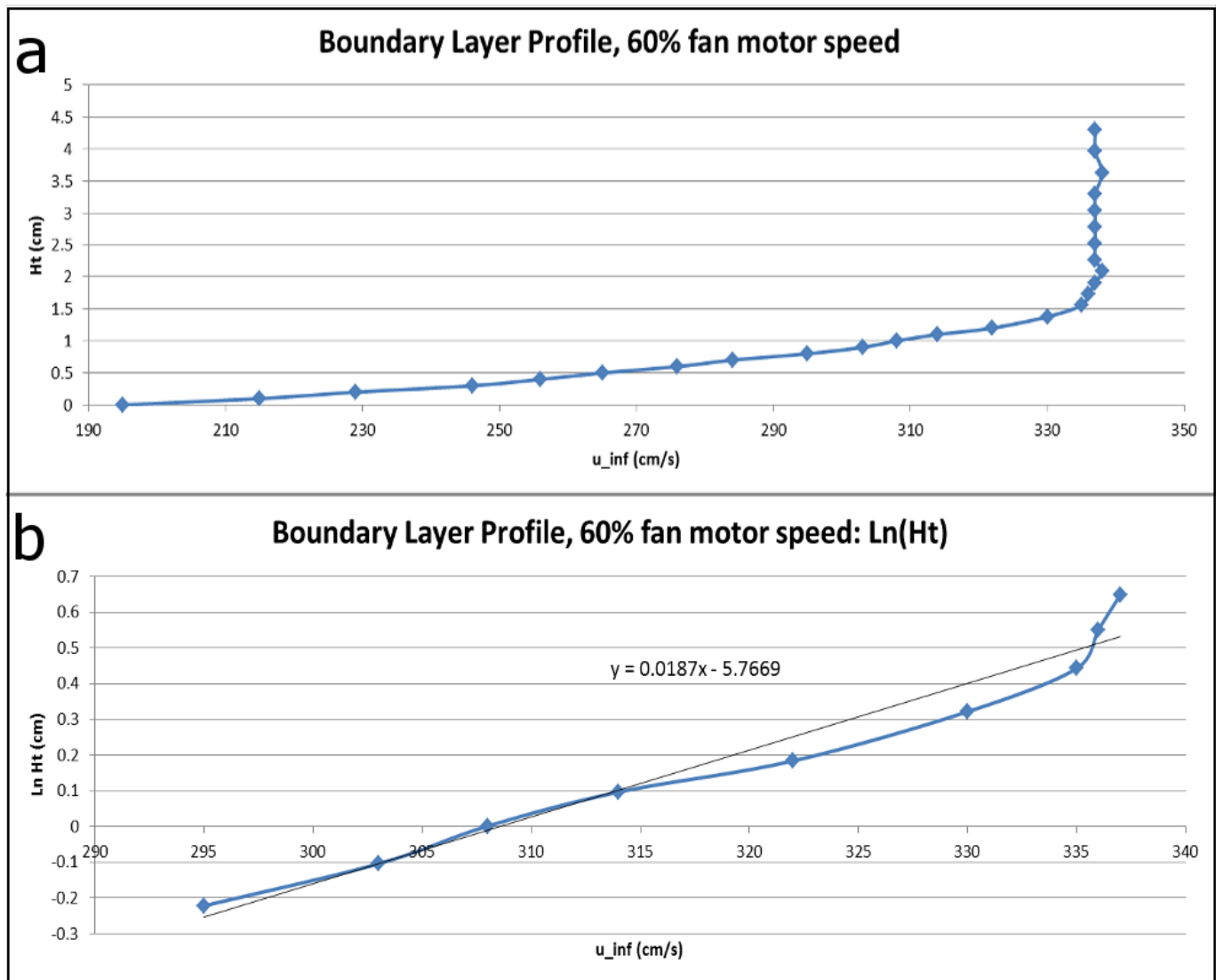


Extended Data Figure 2 | A view into the test section with the test plate inserted. In this photo, the test plate is prepared for an experimental run with silica sand.



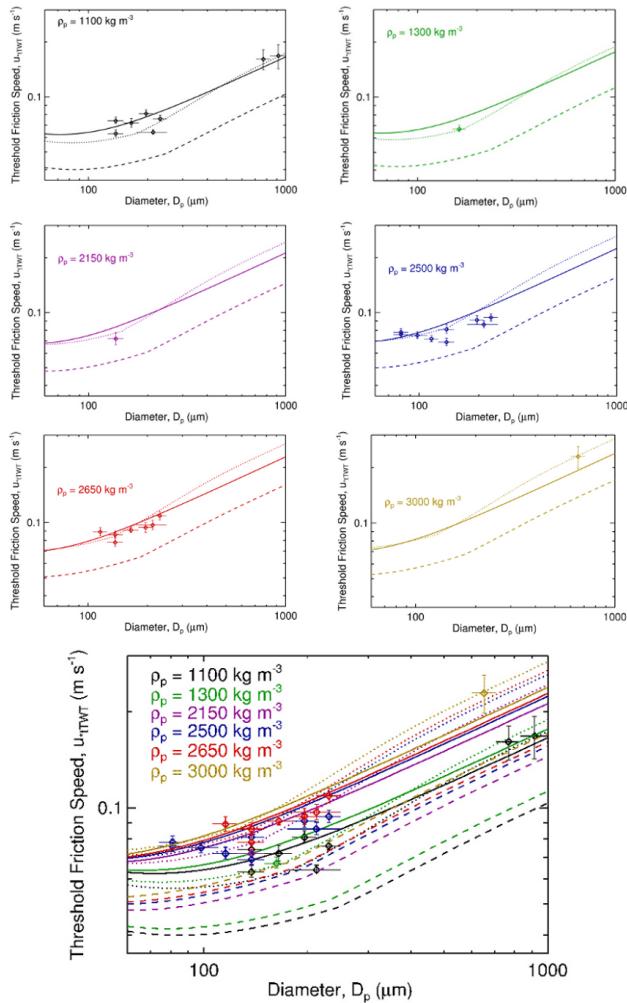
Extended Data Figure 3 | Close-up views of some wind tunnel elements.
a, View of the downwind end of the test section rolled out from the wind tunnel, showing the single upwind viewing port (far left) and the three downwind viewing ports (top of third port visible on far side of test section). The downwind end of the calibration plate is seen within the test section (lower right), with walnut shell and pneumatic lines visible (traversable pitot tube

within test section not visible). **b,** Oblique view of downstream end of test plate after partial removal from the test section (opening visible at far left) showing the traversable pitot tube assembly (in centre of photo). 100-grit (125 µm-diameter grains) sandpaper, for ensuring development of a representative boundary layer, is visible to the left (upwind side) of the pitot tube assembly.

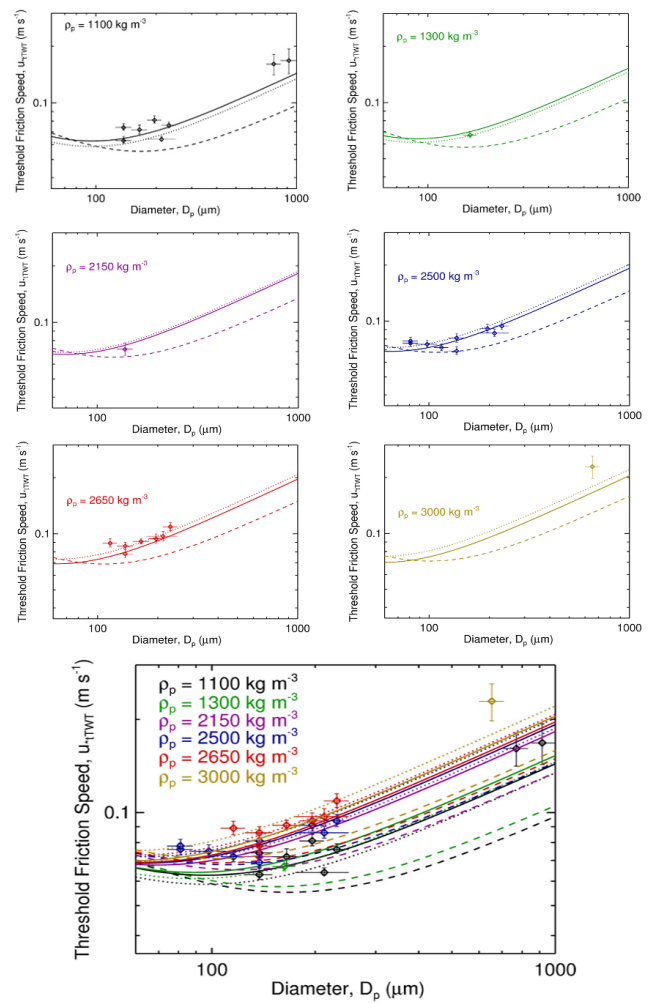


Extended Data Figure 4 | Example plot (at 60% of the maximum rated fan motor speed) of boundary layer data collected with the traversable pitot tube. **a**, Data showing that the boundary layer is fully developed with a freestream wind speed, $u(z)$, of $\sim 3.35 \text{ m s}^{-1}$ at a height of ~ 1.9 cm.

b, Linearized data illustrating how values of roughness height (z_0) are derived. Fitting a straight line to the data gives the equation $y = 0.00187x - 5.7669$ in centimetres. Comparison with equation (5) shows that $\ln(z_0) = -5.7669$, such that $z_0 = \sim 0.003$ cm.

TWT: Iversen and White,
modified

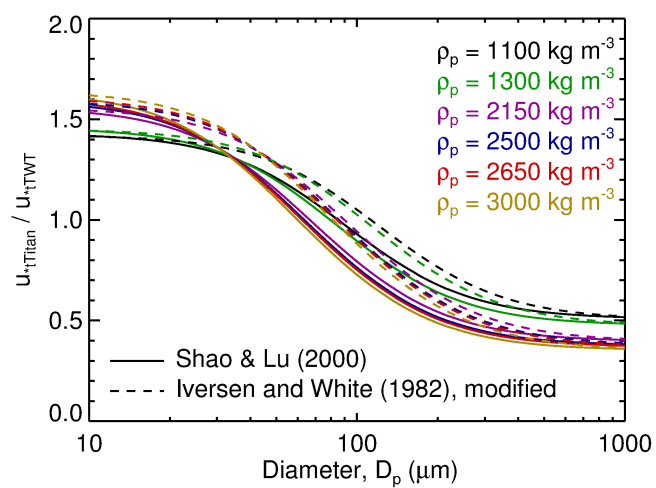
TWT: Shao and Lu



Extended Data Figure 5 | Plots of experimentally derived threshold friction wind speeds in the TWT for the Iversen–White and Shao–Lu models.

For each plot, the dashed line represents the nominal model, the solid line shows the model matched to the data using the density ratio term of ref. 8, and the dotted line shows the model fitted to the data (χ^2 minimization). For the modified Iversen–White model, we use $K = 0.055 \text{ g s}^{-2}$ and $n = 2$ (following ref. 8; see Extended Data Table 4). This modification makes the interparticle force (I_p) proportional to D_p as in the Shao–Lu model⁷, thereby facilitating comparison between the two models. The modified Iversen–White model⁶ is plotted for their equations 5 ($0.03 \leq \text{Re}_p^* \leq 10$) and 6 ($10 \leq \text{Re}_p^*$) (see

equations (7) and (8) here), with the transition between the two particle friction Reynolds number regimes at $\sim 200 \mu\text{m}$. The Shao–Lu model⁷ is plotted for their nominal value for A_N (0.0123) and for their lowest value for γ ($1 \times 10^{-4} \text{ kg s}^{-2}$) to optimize the fit. The proximity of the models with the density ratio term (solid lines) and the models fitted to the data (dotted lines) indicates the power of the density ratio term to match the models to the data. Horizontal bars indicate the range of grain sizes (Extended Data Table 2). Vertical bars show the standard deviation uncertainty in speed for the number of data points indicated in Extended Data Table 2; see Methods for calculation of uncertainties.



Extended Data Figure 6 | Plot of the u_{tTitan}^* ratios used for converting the u_{tTWT}^* to u_{tTitan}^* . See Methods ('Comparison of u_{tTitan}^* with models') for details.

Extended Data Table 1 | Conditions necessary to achieve similitude of kinematic viscosity with the Titan near-surface atmosphere

PARAMETER	TITAN	TITAN WIND TUNNEL
Atmospheric composition	~95% N ₂ , ~5% CH ₄	~79% N ₂ , ~20% O ₂
Static pressure, P (Pa)	1.44×10^5	1.25×10^6
Temperature, T (K)	94	293
Molecular (dynamic) viscosity, μ (Pa s) ^a	6.25×10^{-6}	1.85×10^{-5}
Atmospheric Density, ρ (kg m ⁻³) ^b	5.3	14.5
Kinematic viscosity, ν (m ² s ⁻¹) = μ / ρ	1.2×10^{-6}	1.2×10^{-6}

Extended Data Table 2 | Experimental matrix of sediments with 23 unique combinations of particle diameter (D_p) and density

Material	Density D_p (kg m ⁻³)	Density D_p (microns)	Average D_p (microns)	Date (YYYY)	Error	$u_{d(fixed)}$	$u_{d(TWT)}$	$u_{d(TWT)}^*$	$u_{d(Titan)}^*$			
					Value (s.d.)					n	units for all wind speeds are m s ⁻¹	
Walnut shell	1100	125-150	138	2012	+3.1%	3	0.99	1.04	0.063	0.058		
					-3.0%							
				2013	+2.7%	1	1.11	1.23	0.074	0.068		
					-2.7%							
		150-180	165	2013	+3.5%	2	1.10	1.21	0.072	0.060		
					-3.5%							
		180-212	196	2013	+5.1%	3	1.19	1.34	0.081	0.063		
					-5.1%							
175-250	213	2012	+3.4%	3	1.00	1.06	0.064	0.048				
			-3.4%									
GC *	1300†	150-175	163	2012	+3.2%	3	1.03	1.11	0.067	0.054		
					-3.2%							
		125-150	138	2013	+7.2%	3	1.09	1.20	0.072	0.056		
					-7.2%							
		Glass spheres (solid)	2500	74-88	81	2012	+3.6%	4	1.14	1.27	0.076	0.078
							-3.6%					
						2013	+3.7%	2	1.16	1.29	0.078	0.080
							-3.7%					
88-106	97			2013	+5.1%	3	1.13	1.26	0.075	0.069		
					-5.1%							
106-125	116			2013	+4.5%	3	1.10	1.21	0.072	0.060		
					-4.4%							
125-150	138	2012	+3.6%	3	1.06	1.15	0.069	0.052				
			-3.6%									
Silica Sand	2650			2013	+4.2%	3	1.20	1.36	0.081	0.061		
					-4.2%							
		180-212	196	2013	+3.8%	2	1.30	1.51	0.091	0.055		
					-3.8%							
		175-250	213	2012	+4.1%	3	1.25	1.43	0.086	0.050		
					-4.1%							
		212-250	231	2013	+4.2%	2	1.20	1.36	0.094	0.053		
					-4.2%							
Basaltic sand	3000	106-125	116	2013	+4.7%	3	1.28	1.48	0.089	0.074		
					-4.7%							
		125-150	138	2012	+3.6%	3	1.16	1.30	0.086	0.064		
					-3.6%							
				2013	+5.4%	3	1.24	1.44	0.078	0.058		
					-5.4%							
		150-180	165	2013	+5.6%	2	1.30	1.51	0.091	0.060		
					-5.6%							
180-212	196	2013	+2.8%	1	1.34	1.57	0.094	0.056				
			-2.8%									
175-250	213	2012	+4.8%	2	1.37	1.62	0.097	0.056				
			-4.8%									
212-250	213	2013	+4.9%	3	1.51	1.82	0.109	0.060				
			-4.9%									
Basaltic sand	3000	600-707	654	2013	+13.6%	4	2.85	3.82	0.229	0.087		
					-13.6%							

This distribution of materials includes predominately materials of similar equivalent weight (mass \times gravity) to organic materials of the predicted grain size on Titan, as well as some heavier and larger particles to constrain the threshold curve at higher grain sizes (Fig. 2 and Extended Data Fig. 5). This table also shows the measured and derived threshold wind speeds, where $u_{t(fixed)}$ is the freestream threshold wind speed at the fixed pitot, $u_{t(TWT)}$ is the freestream threshold wind speed in the test section, $u_{t(TWT)}^*$ is the friction threshold wind speed in the test section, and $u_{t(Titan)}^*$ is the friction threshold wind speed on Titan scaled to a particle density of 1,000 kg m⁻³. The error values are calculated as standard deviations (Methods) and are shown in Fig. 2 and Extended Data Fig. 5. n is the number of data points, which is the number of runs for which threshold was observed.

* Gas chromatograph column-packing material.

† Calcined diatomite.

Extended Data Table 3 | Description of each stage of grain motion during data collection

STAGE	DESCRIPTION (<i>focused on the central ~one-third of the bed within the field of view</i>)
<i>INCREASING WIND SPEED</i>	
First motion	The first perception of individual grain motion, including vibrating in place or rolling (observed as twinkling) or saltation
Flurries	Sporadic or episodic grain motion, commonly saltation
Patches	Continuous grain motion but occurring over less than 50% of the bed
50% of bed in motion	Continuous grain motion occurring over ~50% of the longitudinally central portion of the bed in motion → designated as threshold
100% of bed in motion	Continuous grain motion occurring over the entire bed
<i>DECREASING WIND SPEED</i>	
50% of bed in motion	Continuous grain motion occurring over ~50% of the longitudinally central portion of the bed in motion
Patches	Continuous grain motion but occurring over less than 50% of the bed
Flurries	Sporadic or episodic grain motion, commonly saltation
Twinkling	Flashes of sparkling, interpreted as limited or individual grain motion, including vibrating in place or rolling (observed as twinkling) or saltation
No motion	No perceived change in the field of view

Extended Data Table 4 | Values for the interparticle force parameters in various formulations of the models used here

Publication	Parameter	Value	Origin
Iversen et al. 1976, Iversen et al. 1987	K^*	0.055 g s^{-2}	Fitted
	n	2^\dagger	Assumed
Iversen and White 1982, Greeley and Iversen 1985	K^*	$0.006 \text{ g cm}^{0.5} \text{ s}^{-2}$	Fitted
	n	2.5	Fitted
Shao and Lu 2000	γ	0.10 g s^{-2}	Fitted

* For comparison with equation (2), $K = A_d I_p$.

† The value of $n = 2$ results in I_p being proportional to D_p .